

Spiral galaxies with WFPC2: III. Nuclear Cusp Slopes<sup>1</sup>C M .Carollo<sup>2;3;4</sup> & M .Stiavelli<sup>4;5;6</sup>

Received \_\_\_\_\_; accepted \_\_\_\_\_

---

<sup>1</sup>Based on observations with the NASA/ESA Hubble Space Telescope, obtained at the Space Telescope Science Institute, which is operated by Association of Universities for Research in Astronomy, Inc. (AURA), under NASA contract NAS5-26555

<sup>2</sup>Hubble Fellow

<sup>3</sup>Johns Hopkins University, 3701 San Martin Dr., Baltimore, MD 21218

<sup>4</sup>Space Telescope Science Institute, 3700 San Martin Dr., Baltimore, MD 21218

<sup>5</sup>On assignment from the Space Science Dept. of the European Space Agency

<sup>6</sup>On leave from the Scuola Normale Superiore, Piazza dei Cavalieri 7, I56126 Pisa, Italy

## A B S T R A C T

In this paper, the third of a series dedicated to the investigation of the nuclear properties of spiral galaxies, we have (i) modelled the WFPC2 F606W nuclear surface brightness profiles of 41 spiral galaxies presented in Carollo et al. 1997c, 1998 with the analytical law introduced by Lauer et al. 1995, and (ii) deprojected these surface brightness profiles and their analytical fits, so as to estimate the nuclear stellar densities of bulges of spiral galaxies. We find that the nuclear stellar cusps (quantified by the average logarithmic slope of the surface brightness profiles within  $0.1''$ - $0.5''$ ) are significantly different for  $R^{1=4}$ -law and exponential bulges. The former have nuclear properties similar to those of early-type galaxies, i.e. similar values of nuclear cusps for comparable luminosities, and increasingly steeper stellar cusps with decreasing luminosity. By contrast, exponential bulges have (underlying the light contribution from photometrically distinct, central compact sources) comparative shallower stellar cusps, and likely lower nuclear densities, than  $R^{1=4}$ -law bulges.

Subject headings: Galaxies: Spirals | Galaxies: Structure | Galaxies: Fundamental Parameters | Galaxies: Nuclei

## 1. Introduction

The galactic nuclei are the repositories of low angular momentum material sunk to the centers over the lifetime of the parent systems. Therefore, they are likely to hold answers to important questions related with the origin of structure in the parent galaxies. In this perspective, establishing the demographics of galactic nuclei along the entire Hubble sequence lies at the heart of our understanding of the complex process of galaxy formation and evolution.

Observations of nearby ellipticals and lenticulars with the Faint Object Camera (FOC), the Wide Field Planetary Camera (WF/PC) and the Wide Field Planetary Camera-2 (WFPC2) aboard the Hubble Space Telescope (HST) have revealed that the nuclei of these galaxies are complex environments (e.g., Crane et al. 1993; Jaffe et al. 1994; Lauer et al. 1995, hereafter L95; Forbes et al. 1995; Carollo et al. 1997a, hereafter C97a; Carollo et al. 1997b, hereafter C97b; Faber et al. 1997, hereafter F97). They show surface brightness profiles that increase down to the innermost point measurable at HST resolution, i.e.,  $I(r)/r$  as  $r \rightarrow 0$  (where  $I(r)$  is the surface brightness at the radius  $r$ , and  $r > 0$ ); furthermore, several galaxies host stellar and gaseous disks, unresolved nuclear spikes, double nuclei. These inner features might possibly be related to the presence of massive black holes (e.g., Lauer et al. 1996).

By contrast, much is still to be learned about the nuclear properties of nearby spiral galaxies at HST resolution. F97 found that the surface brightness profiles of the three Sa-Sb bulges present in their sample show a behaviour similar to that of early-type spheroidals of comparable luminosity. The same result was found by Phillips et al. (1996) for the three spirals of type earlier than Sc contained in their WF/PC F555W sample of 20 disk galaxies. Furthermore, Phillips et al. found that later type spirals show instead (almost) flat nuclear profiles, and suggested that the nuclear properties of disk galaxies are more closely related to those of nucleated dwarf galaxies than to those of elliptical galaxies. Further exploration is necessary to assess how the nuclear properties scale with the properties of the spheroidal component. This is likely to provide feedback information about the epoch and processes of nucleus, bulge, and, ultimately, galaxy formation.

In order to address these issues, we have performed a WFPC2 snapshot survey in the F606W filter of the nuclei of 107 (mostly Sa to Sc) disk galaxies. In paper I (Carollo et al. 1997c) and paper II (Carollo et al. 1998) we have presented the 75 targets imaged so far within our program. Our analysis shows that bulge-like structures are present in most of the galaxies. While in some cases these are "classical", smooth, featureless  $R^{1=4}$ -law bulges, in others they are better fitted by an exponential profile (see also Courteau, de Jong & Broeils 1996, and references therein, for similar results). The exponential bulges include two classes of objects: (i) dwarf-looking systems, whose surface brightness profiles within  $15''$  are well fitted by a single exponential. These galaxies are strongly bulge-dominated; their surrounding, faint regions ("disk/halo") show no signs of spiral arms, and have typically a quiescent, i.e. non star forming, appearance. (ii) Small exponential bulges embedded in dominant (spiral-armed/star-forming) surrounding disks, i.e., the inner exponential structures of double-exponential fits to the surface brightness profiles within  $15''$ . The exponential bulges as-a-class are statistically fainter than the featureless, smooth  $R^{1=4}$  bulges, for constant disk luminosity and Hubble type. Resolved, central compact sources are found in most of the exponential bulges; the hosts of central compact sources often contain a barred structure. The nature of these compact source, and in particular their relation with e.g., star clusters and Seyfert 2 nuclei, is discussed in Carollo (1998).

In this paper, the third of the series, we investigate the relation between the nuclear structure of spiral galaxies and the physical properties of inner disks and/or bulges. In particular, we (i) present the results of modeling the nuclear surface brightness profiles with the analytical law introduced by L95 (for the 43 galaxies of paper I and II for which we could perform the measurements), (ii) deconvolve the surface brightness profiles and their analytical fits in order to estimate the nuclear stellar densities, (iii) study the nuclear properties as a function of the global properties discussed in papers I and II (e.g.,  $R^{1=4}$  against exponential bulges), and (iv) compare the nuclear properties of our sample with those observed in early-type galaxies. The paper is organized as follows. In section 2 we briefly summarize the properties of the sample, the data used in our investigation, the procedure adopted for the data reduction, and the steps performed to derive the surface brightness profiles. In section 3 we present the results of the analytical

ts applied to the surface brightness profiles, and of deconvolving data and models in spherical symmetry. In section 4 we investigate the dependence of the nuclear properties on global galactic properties. We conclude in section 5.

## 2. The Sample, the Data and the Data Reduction

We address to papers I and II for details on the selection of the total sample, the data, and the procedure adopted for their reduction. Below we briefly summarize the important points.

We selected a total of 92 spiral galaxies (from the UGC catalog for the northern hemisphere, Nilson 1973, and from the ESO IV catalog for the southern hemisphere, Lauberts & Valentijn 1989), which satisfy the following constraints: (i) Angular diameter larger than 1 arcmin; (ii) Regular types Sa, Sab, Sb, and Sbc; (iii) Redshift  $< 2500$  km/s, to guarantee a high angular resolution in physical size; (iv) An inclination angle, estimated from the apparent axial ratio, smaller than 75 degrees. Fifteen additional galaxies were chosen among E/S0 and S0/Sa, so as to have a reference sample for comparison with the literature on early-type galaxies. In this paper we use the surface brightness profiles of the 18 objects presented in paper 1, and of the 25 objects presented in paper 2, for which the light distribution was regular enough to allow us to perform the measurements. Some parameters for the total sample of 43 galaxies studied in this paper are given in Table 1. We adopt  $H_0 = 65$  km/s/Mpc throughout this paper.

For each galaxy we acquired two WFPC2 F606W exposures of 400 and 200 seconds, respectively. The observations were taken with (gain 15 and) the galaxy nucleus centered on the PC, which has a scale of  $0.046'' \text{ px}^{-1}$ , and a useful field of about  $35'' \times 35''$ . The observations were carried out in one lock. The data reduction included: (i) the reprocessing of the raw images with the standard WFPC2 pipeline in order to use the most recent reference frames for flat fielding, bias and dark current subtraction; (ii) the addition and cosmic-ray cleaning of the two images by using the IRAF/STSDAS task `ccrej`; (iii) the removal of remaining hot pixels by interpolation; (iv) sky subtraction by determining the sky values from the WFC images, in areas furthest from the

nucleus. The derivation of the surface photometry was carried out in IRAF. For the sample of paper I, we used two different ellipse-fitting programs (\Galphot", Franx, Illingworth & Heckman 1989, and \Ellipse", R. Jedrezjeski), and two different approaches for the dust- and star-masking, so as to have an estimate of the uncertainties introduced by the complex dust and star-forming structures. Both approaches only correct for patchy dust absorption and not for any smooth and extended dust component, which remains undetectable in our data. For the sample of paper II, we only used the task \Ellipse", since the previous study shows that the two packages give equal results within the errors. Absolute photometric calibration was obtained by applying the zero-point for the F606W filter provided by Holtzman et al. (1995), i.e.

$$m_{\text{agF606W}} = 2.5 \log(\text{counts} \cdot \text{sec}) + Z_{\text{WFPC,F606W}} + 5 \log(0.046) + 0.1 \quad (1)$$

with the zero-point  $Z_{\text{WFPC,F606W}}$  equal to 22.084. The subsequent term accounts for the pixel size. The constant shift of 0.1 mag was added following Holtzman et al. in order to correct for finite aperture. This calibration provides a rough conversion to V-Johnson magnitudes (i.e., in average within 0.2 magnitudes, given the difference in bandpass between the Johnson V and the F606W filters, and the lack of a color term for our sample). The calibrated surface brightness profiles were corrected for Galactic extinction by using the values published by Burstein & Heiles (1984).

### 3. Analytical Fits to the Nuclear Surface Brightness Profiles

One of the main purposes of any analytical description of the light detected from astronomical sources is to provide a simple way to quantify the most relevant features and their variations from object to object within the same family of sources, and to compare these features among objects of different families. For the early-type galaxies, a popular description of the surface brightness profile has been proposed by L95, and used by Byun et al. (1996) to describe the nuclear properties

of kinematically normal early-type galaxies, and by C 97a, C 97b to describe those of elliptical galaxies with kinematically-distinct cores. It reads:

$$I(r) = 2^{(\gamma - \beta)} I_b \left(\frac{R_b}{r}\right)^h \left[1 + \left(\frac{r}{R_b}\right)^{2(\beta - \gamma)}\right]^{-1} \quad (2)$$

The parameter  $R_b$  is the break radius at which, in giant elliptical galaxies, the profile attains to a more shallow (but always non-zero) slope,  $\beta$  is the slope of the inner profile (i.e.,  $I(r) \propto r^{-\beta}$  as  $r \rightarrow 0$ ),  $\gamma$  is the slope of the outer profile,  $h$  controls the sharpness of the transition between inner and outer profile, and  $I_b$  is the surface brightness at  $R_b$ . The profile of equation (2) provides an adequate description of the features present in the surface brightness profiles of early-type galaxies along their entire luminosity sequence.

The structure that we detect in the nuclei of several disk galaxies requires a clear definition of what are the relevant features in these galaxies that we aim at quantifying. In particular, for the exponential galaxies which host a perfectly centered compact source, there is a conceptual choice which has to be made, namely whether to include the central source in the analytical description of the galaxy (in a few galaxies, the "central" compact source reported in Table 1 is actually slightly offset from the center of the outer isophotes. Therefore, it has not been considered in the isophotal fitting, and does not appear in the surface brightness profile). In principle, these systems could be described by an exponential profile modified to include a steep nuclear cusp slope. In order to check whether this is a physically acceptable solution, we fitted the exponential-bulge galaxies hosting a central compact source with a light profile described by:

$$I(R) = I_0 \left[1 + \frac{R_c}{R}\right]^{-\alpha} \exp(-R/R_s) \quad (3)$$

For radii  $R$  much smaller than the "cusp" radius  $R_c$ , this profile describes a cusp with slope  $\alpha$ .  $I_0$  is the central brightness of the exponential component, and  $R_s$  the exponential scalelength. No acceptable (i.e., physically meaningful) fit could be found for any galaxy except ESO 499 G 37. This demonstrates that "steep-cusp exponentials" could indeed exist, and that our procedure would be able to identify them. However, the fact that they generally do not provide a good or

meaningful it supports the interpretation, based on morphology, that central compact sources are photometrically distinct components from their surroundings, and not simply a steepening of the light profile. On this basis, we considered these sources as an additional contribution to the to-be-fitted, underlying galaxy light. The radial profile of the latter is what can be meaningfully compared to the radial profile measured for the early-type systems. Indeed, the same choice was made by Byun et al. (1996), who excluded from their fits the light excess from the resolved nuclei embedded in the bulges of a few galaxies of their sample (e.g., NGC 1331, NGC 3599, NGC 4239). Therefore, in order to perform a direct comparison with elliptical and lenticular galaxies, we adopted equation (2) to describe the nuclear properties of spiral galaxies. Some details on the analytical "L95 fits" are given in Appendix A.

There is an intrinsic uncertainty in disentangling the contribution of the nuclear compact source from the unknown underlying galaxy light. In order to quantify this uncertainty, we performed several fits to the same galaxy, by considering different inner radial cutoff in its surface brightness profiles. The resulting inward extrapolations of the best fits to the outer points may differ significantly, but are likely to bracket the true shape of the underlying galactic light, free from PSF-blurring and central compact source contamination. We were able to fit 41 of the 43 galaxies (for the two remaining objects, ESO 205G 7 and NGC 3177, no acceptable fit was obtained). In Figure 1 we show the surface brightness profiles, and the fits with the Point Spread Function (PSF) convolved models, for the 41 galaxies. In Table 2 we list, for each galaxy, radial range adopted for performing the fits, and the corresponding best fit values for  $R_b$ ,  $\alpha$ ,  $\beta$ , and  $\mu_b = -2.5 \log I_b$ . For those objects for which changing the radial range for the fits lead to significantly different solutions, we show in the table and in the figure the two "bracketing" fits.

For each galaxy, the analytical fits to the surface brightness profiles were used to derive the average logarithmic nuclear slopes  $\beta$  corrected for PSF and central compact source effects. The average slopes provide a global representation of the underlying projected galactic light within a defined radial range. This was taken equal to  $0.1^0\text{--}0.5^0$  (similarly to what was done by L95 and C97a for the early-type systems), which corresponds to physical scales smaller than  $\sim 100$  pc



at the average distance of the galaxies ( $\sim 25$  Mpc). In contrast to the values of the individual parameters in the best fits, which for the same galaxy can differ significantly from one best fit to the other (obtained within different radial ranges), the  $h_i$  values provide a robust description of the nuclear surface brightness profiles contributed by the underlying galactic light. For the galaxies for which two fits are presented, we adopted the arithmetic mean of the corresponding values of  $h_i$ . An estimate of the uncertainty associated with these measurements is given by the difference between the two values, and is typically smaller than  $\sim 0.2$ . The values of the average logarithmic slopes inside  $0.1^{00}$ - $0.5^{00}$ ,  $h_i$ , are also listed in Table 2.

### 3.1. Deprojections

The analytical fits to the surface brightness profiles were deprojected in spherical symmetry by means of an Abel inversion (Binney & Tremaine 1987), to derive the luminosity density profiles  $\rho_{\text{mod}}(r)$ . The same was done using directly the data points  $[_{\text{data}}(r)]$ . Despite the fact that the deprojection amplifies the fluctuations and errors present in the data, and although the deprojection of the data introduces systematic errors due to the effects of the WFPC2 PSF, at radii of  $r' \sim 0.1^{00}$  (where the effects of the WFPC2 PSF are modest) the comparison between  $\rho_{\text{mod}}(r)$  and  $_{\text{data}}(r)$  provides a rough estimate for the effect of the central compact source on the underlying stellar density, and more generally an estimate for the uncertainty associated with the measurements.

In order to quantify the general accuracy of this estimate, and in particular the effects of the WFPC2 PSF, we carried out the following test. For the galaxies which do not host a central compact source, we started from their (PSF-free) L95 models, deprojected both these "intrinsic" profiles and those obtained from them after convolution with the WFPC2 PSF, and compared the corresponding densities at  $0.1^{00}$ . The deprojections of the intrinsic and PSF-convolved profiles yielded densities at  $0.1^{00}$  (or 10 pc) within 10-15%. For the exponential galaxies which host a central compact source, we added to their (PSF- and compact source-free) L95 models a central

source described by a Plummer model of varying radius, in order to also assess the effect of such a light concentration on the central densities. We then repeated the same steps described above, i.e., deprojected these intrinsic profiles and those obtained after PSF-convolution, and compared the resulting densities at  $0.1''$ . In this case, the comparisons showed that for the range of compact source luminosities and radii observed in our sample, the straight deprojection of the data, ignoring the effect of the HST PSF, can be in error by up to a factor 50% (see Figure 2, where we plot, as an example, the results for ESO 482G 17). This error is much smaller than the effect of the compact source itself, which typically increases  $\rho_{0.1''}$ ,  $_{10\text{pc}}$  of a factor ten or more.

The deprojected luminosity density profiles are shown in Figure 3, where the deprojections of the  $\rho_{\text{mod}}$  are plotted as solid lines, and those from the data ( $\rho_{\text{data}}$ ) as dashed lines. When two analytical descriptions were available for the same galaxy, in Figure 3 we plot the deprojection corresponding to the first of the two fits in Table 2. The values of the stellar densities at  $0.1''$  and at 10 pc derived from deprojecting the data ( $\rho_{\text{data};0.1''}$  and  $\rho_{\text{data};10\text{pc}}$ , respectively) and the models ( $\rho_{\text{mod};0.1''}$  and  $\rho_{\text{mod};10\text{pc}}$ , respectively) are given in Table 3.

In the remainder of this paper, we use the values of  $\rho_{\text{data};0.1''}$ ,  $\rho_{\text{mod};0.1''}$  and  $h_i$  to describe the nuclear properties of disk galaxies. The choice of using the densities at  $0.1''$  rather than those at 10 pc is justified by the fact that the latter, although more physically motivated, often probe a radius smaller than the typical FWHM of the PSF. Nonetheless, we have checked that our main results remain unchanged when the densities at  $0.1''$  are substituted with those at 10 pc. For those objects for which two values of  $\rho_{\text{mod};0.1''}$  were available, we adopted the smallest of the two. This choice maximizes the estimate for the associated errorbar, since in these objects typically  $\rho_{\text{data};0.1''} > \rho_{\text{mod};0.1''}$ .

#### 4. Discussion

The HST exploration of the nuclei of nearby early-type galaxies has highlighted the diversity between low-luminosity, rotation-supported, radio-quiet, disk-isophote galaxies, and

high-luminosity, pressure-supported, radio-loud, boxy-isophote systems. The diversity holds in fact down to the tens-of-parsecs scales: the former have power-law (steep-cusp) light profiles and high stellar densities; the latter show a break radius inside which the profile attens to a shallow (but non-zero) cusp slope, and have low-density nuclei (e.g., L95). It is unclear however whether the connection between small and large scale properties in early-type spheroidals is operated by nature, i.e. it is the outcome of a different formation epoch, time scale or physical mechanism, or is operated by nurture, i.e. it results from subsequent galactic evolution. In the orthodox framework where bulges of spiral galaxies are the extrapolation of the spheroidal family toward fainter magnitudes, and in the light of the variety of structural properties shown by the central spheroidal structures embedded in disk galaxies (e.g., Komendy 1993; Courteau et al. 1996; papers I and II), the differences and similarities between the nuclear properties of (i)  $R^{1=4}$ -law versus exponential bulges, and (ii) bulges versus higher luminosity spheroidals, can provide important feedback toward understanding the processes involved in the formation of spheroidals and their nuclei.

In Figure 4 we plot the average nuclear slope inside  $0.1^{0.5^{0}}$ ,  $h_i$ , versus the total F606W magnitude of the spheroidal component  $M_{F606W}$ . Triangles represent galaxies fitted by a single exponential, pentagons those fitted by two exponentials, circles the  $R^{1=4}$ -law bulges, and asterisks the early-type galaxies of L95, F97 (small symbols), and C97a, C97b (large symbols). Only 33 of the 41 bulges for which we could derive the measurements of  $h_i$  appear in the figure: for seven of the remaining eight objects, no measurement of  $M_{F606W}$  was available (see Table 1, galaxies labelled by "NGF" in the last column {ESO 205G 7 is not included in these seven objects, since for it neither  $M_{F606W}$  nor  $h_i$  could be derived}); furthermore, we excluded NGC 488 from the plots since its measurement of  $M_{F606W}$  is uncertain (although it definitely shows an  $R^{1=4}$ -law profile, see Figures 6 and 8). We verified that the inclusion of NGC 488 in our analysis does not change our conclusions.

There is a clear dichotomy between  $R^{1=4}$ -law and exponential bulges, which holds even when only exponential bulges embedded in otherwise normal outer disks (pentagons) are considered. The  $R^{1=4}$ -law bulges lie on the  $h_i$  versus absolute bulge magnitude relation traced by early-type

galaxies of similar luminosities, i.e. the fainter the bulge, the steeper its nuclear stellar cusp. By contrast, exponential bulges (extend to fainter magnitudes and) have significantly shallower stellar cusps for a given luminosity. It is true that these typically underly the light contributed by a central compact source, and are therefore subject to a larger uncertainty; however, the dichotomy remains even within the most conservative assumptions for the error bars. The effect is likely not one of "evolution" along the Hubble sequence, since we compare mostly galaxies of similar and intermediate, i.e. Sb to Sc, Hubble type (see Figure 5, where we plot the average nuclear slope inside  $0.1^{00}$ - $0.5^{00}$ ,  $h_i$ , versus Hubble type, from RC3). In Figure 5, NGC 488 is included as a  $R^{1=4}$ -law bulge, while NGC 3928, ESO 548G 29, ESO 240G 12 and ESO 482G 17 are excluded, due to their uncertain morphological classification. The six squares in Figure 5 (absent in Figure 4) correspond to those galaxies for which no good fit to a bulge component could be derived, but for which the measurement of  $h_i$  could be performed (all galaxies { excluding NGC 3928 { labelled with "NGF" in the last column of Table 1).

A main question is whether the difference in nuclear slopes between  $R^{1=4}$ -law and exponential bulges carries important information about the structure (and formation) of these systems, or is rather a trivial result which simply states the difference between an inward extrapolation of an  $R^{1=4}$ -law and an exponential profile. The bulge parameters presented in papers I and II were obtained from fits in the range  $0.5^{00}$  to the last measured point: using the largest radial range available was found to provide an overall better fit to the data. However, performing the  $R^{1=4}$ -law and exponential fits after excluding the data inside the innermost  $1^{00}$  demonstrates that there is no ambiguity outside such radius between  $R^{1=4}$ -law and exponential bulges: the classification of a bulge as an  $R^{1=4}$ -law or an exponential structure holds on a radial range entirely different from the  $0.1^{00}$ - $0.5^{00}$  used in the derivation of the average nuclear slopes  $h_i$  (see Appendix B for further details). This strongly supports the interpretation that exponential bulges have intrinsically shallower cusp slopes than  $R^{1=4}$ -law structures. In Figure 6 we show the L95 fits (dotted lines), and the single bulge or bulge plus disk fits (solid lines), for four representative objects, i.e., a single exponential (ESO 482G 17) or  $R^{1=4}$ -law (NGC 488) bulge, a two-exponentials galaxy (ESO 498G 5), and a  $R^{1=4}$ -law plus exponential object (NGC 2344). When a two-components fit is required, we also

plot the bulge (short-dashed lines) and disk (long-dashed lines) components separately. The total (bulge plus disk) fits and the bulge components overlap at small radii. These examples clearly illustrate that while the L95 fits are aimed at representing the innermost galactic regions, the bulge (plus disk) fits are aimed at matching the outer profiles.

The deprojected stellar density at  $0.1''$  versus absolute magnitude of the bulge component  $M_{F606W}$  is shown in Figure 7. The symbols (as in Figure 4) represent the measurements derived from the deprojections of the analytical fits of Table 2 ( $\rho_{mod;0.1''}$  in Table 3). For those galaxies whose deprojection of the surface brightness profile gives a stellar density  $\rho_{data;0.1''}$  which is significantly larger than  $\rho_{mod;0.1''}$ , an arrow is plotted, which connects the value of  $\rho_{mod;0.1''}$  to the corresponding value of  $\rho_{data;0.1''}$ . The spherical deprojections might underestimate the density for large intrinsic flattening. Assuming that the exponential bulges have flattening comparable with that of the  $R^{1=4}$ -law bulges, these structures have nuclear stellar densities underlying the central compact sources which are at the low-end side of those of early-type spheroidals and  $R^{1=4}$ -law bulges. Exponential bulges might therefore break the general trend of "classical" spheroidals, i.e., to have a higher density the lower the luminosity. The "dichotomy" in nuclear properties between exponential and  $R^{1=4}$ -law bulges constitutes an additional piece of the puzzle concerning "how and when" bulges form. A discussion on the possible implications of our results for scenarios of bulge formation (generally supporting the idea that there is present-day "bulge-formation" in the centers of spirals through bar-driven inflow of dissipative material; e.g., Combes et al. 1990; Hasan, Pfenniger & Norman 1993; Norman, Sellwood & Hasan 1996) is beyond the scope of this paper, and is presented in Carollo (1998).

## 5. Conclusions

In this paper we have investigated the relation between the nuclear structure of spiral galaxies and the physical properties of their bulges. In particular, we have (i) modelled the WFPC2 F606W nuclear surface brightness profiles of 41 spiral galaxies with the analytical law introduced by

L95 (data from papers I and II), and (ii) deconvolved the surface brightness profiles and their analytical fits in order to estimate the nuclear stellar densities of disk galaxies.

Our main result is that  $R^{1=4}$ -law bulges and exponential bulges have significantly different nuclear stellar cusps and densities. Specifically,  $R^{1=4}$ -law bulges have steep stellar cusps which steepen with decreasing luminosity; furthermore, their stellar cusp slopes and densities are similar in values to those of early-type systems of comparable luminosity. By contrast, in exponential bulges, the inward extrapolations underlying the light from the compact sources which sit in their very centers imply rather shallow stellar cusps and, very likely, relatively low nuclear stellar densities.

#### Acknowledgements

We heartily thank Tim Heckman and Colin Norman for helpful discussions, and the anonymous referee for constructive comments to an earlier version of this paper. CMC is supported by NASA through the grant HF-1079.01-96a awarded by the Space Telescope Institute, which is operated by the Association of Universities for Research in Astronomy, Inc., for NASA under contract NAS 5-26555. This research has been partially funded by grant GO-06359.01-95A awarded by ST ScI, and has made use of the NASA/IPAC Extragalactic Database (NED) which is operated by the Jet Propulsion Laboratory, Caltech, under contract with NASA.

#### Appendix A. Details on the Analytical Fits

We used the same fitting procedure described in C97a; we address to this reference for further information. This was carried out in two steps: (1) The first step isolated primary from secondary minima of  $\chi^2$ . The  $\chi^2$  values were computed on a grid of points uniformly distributed on a wide hypercube in parameter space (with dimension equal to the number of free parameters). Once a minimum value was found, a new, smaller, hypercube was placed on that location, and the

procedure iterated. (2) The minimum value found on the hypercube was then used as starting point to initialize a downhill simplex minimization. We tested the procedure on simulated data, and verified that it recovered the initial values with high accuracy. We accepted as final the fits associated with the absolute minimum of  $\chi^2$ .

Deconvolutions of WF/PC data have been proven to be very reliable (e.g., L95). However, in our analysis, we chose not to apply any deconvolution to the post-refurbishment WFPC2 images, and to correct for PSF-blurring while modeling the light profiles. Therefore, the models were convolved with the appropriate PSFs before being compared to the data. Since pointlike sources with adequate S/N located near to the nuclei were not available for most of the galaxies, we computed the PSFs by running Tinytim (Krist 1992). Focus drifts and breathing modify the PSF profile and affect the flux within a 1 PC pixel radius up to 10% (and within 5 PC pixels up to 5%; Suchkov & Casertano 1997). Therefore, the simulated PSFs obtained by construction at the nominal focus position are in principle of similar quality than PSFs derived from archival stars. Furthermore, our approach of convolving the models rather than deconvolving the data minimizes the effects of using a possibly non-perfect PSF.

## Appendix B. Classifying $R^{1=4}$ -law or exponential bulges outside $1''$

In order to ensure that the classification of a bulge as an  $R^{1=4}$ -law or an exponential structure is valid on a radial range entirely different from that used in the derivation of  $h_i$  (equal to  $0.1''$ - $0.5''$ ), we performed as a test the  $R^{1=4}$ -law and exponential fits after excluding the data inside the innermost  $1''$ . This value is a compromise between a radius large enough to exclude the range where  $h_i$  is computed, and small enough to still allow the detection of the small, disk-embedded exponential bulges (pentagons in the figures). As an example, the results of the test are illustrated in Figure 8 for the same four galaxies presented in Figure 6. The solid lines represent either a single exponential (left panels) or a double exponential (right panels) fit; the dashed lines represent either a single  $R^{1=4}$ -law (left panels) or an  $R^{1=4}$ -law plus exponential (right panels)

t. Two different scales are used for the abscissa for the galaxies in the left and right panels, consistently with the different scales of their bulge components. An offset of two magnitudes has been applied to ESO 482G 17 for plotting purposes. There are two important points to note: (i) the kind of profile which provides the bulge classification given in papers I and II, i.e. exponential or  $R^{1=4}$ -law, still provides a better fit to the inner galactic regions, even when the innermost  $1''$  is excluded from the fits; (ii) the alternative profile with respect to the one that provides the classification given in papers I and II generally provides (not only a worse fit but also) physically meaningless best fit parameters (e.g., for ESO 482G 17, the  $R^{1=4}$ -law best fit of Figure 8 has an  $R_e = 385''$ ). We conclude that the distinction between  $R^{1=4}$ -law and exponential bulges holds in a radial range which excludes the one used to derive  $h_i$ , and that the difference in nuclear cusp slopes  $h_i$  between  $R^{1=4}$ -law and exponential bulges has a physical origin. We retained the bulge parameters presented in papers I and II for our discussion, since those fits gave an overall better description of the profiles.



# REFERENCES

- Binney, J., & Tremaine, S., 1987, *Galactic Dynamics*, Princeton University Press, NJ
- Burstein D., Heiles C., 1984, *ApJS*, 54, 33
- Byun, Y.-I., Grillmair, C.J., Faber, S.M., Ajhar, E.A., Dressler, A., Komendy, J., Lauer, T.R., Richstone, D., Tremaine, S., 1996, *AJ*, 111, 1889
- Carollo C.M., Franx M., Illingworth G.D., Forbes D., 1997a, *ApJ*, 481, 711 (C97a)
- Carollo C.M., Danziger, I.J., Rich, M., Chen, X., 1997b, *ApJ*, 491, 545 (C97b)
- Carollo C.M., Stiavelli, M., de Zeeuw, P.T., Mack, J., 1997c, *AJ*, in press (Dec issue, paper I)
- Carollo C.M., Stiavelli, M., Mack, J., 1998, *AJ*, submitted (paper II)
- Carollo C.M., 1998, submitted to *ApJL*
- Combes F., D'ebbasch, F., Friedl, D., P'enniger, D., 1990, *A & A*, 233, 82
- Courteau, S., de Jong, R.S., Broeils, A.H., 1996, *ApJ*, 457, L73
- Crane, P., et al., 1993, *AJ*, 106, 1371
- de Vaucouleurs G., de Vaucouleurs A., Corwin H.G. Jr., Buta R.J., Paturel G., Fouque P., 1991, *Third Reference Catalog of Bright Galaxies*, (New York: Springer Verlag) (RC3)
- Faber S.M., et al., 1997, *Lick Observatory preprint* (F97)
- Forbes, D.A., Franx, M., Illingworth, G.D., 1995, *AJ*, 109, 1988
- Franx M., Illingworth G., Heckman T., 1989, *AJ*, 98, 538
- Hasan H., P'enniger D., Norman C., 1993, *ApJ*, 409, 91
- Holtzman, J.A., Burrows, C.J., Casertano, S., Hester, J.J., Trauger, J.T., Watson, A.M., W'orthey, G., 1995, *PASP*, 107, 1065
- Jaffe W., Ford H.C., O'Connell R.W., van den Bosch F.C., Ferrarese L., 1994, *AJ*, 108, 1567

- Kormendy J., 1993, IAU Symposium 153, Galactic Bulges, eds H.J. Habing, H.B. Dejonghe  
(Dordrecht: Kluwer), p. 209
- Krist, J., 1992, Tinytim v2.1 User's Manual (ST ScI)
- Lauberts A., Valentijn E.A., 1989, The Surface Photometry Catalog of the ESO-Uppsala Galaxies,  
ESO
- Lauer T., et al., 1995, AJ, 110, 2622 (L95)
- Lauer, T.R., et al. 1996, ApJ, 471, L79
- Nilson, P., 1973, Uppsala General Catalog of Galaxies, Uppsala Astron. Obs. Ann., 6
- Norman C.A., Sellwood J.A., Hasan H., 1996, ApJ, 462, 114
- Phillips A.C., Illingworth G.D., Mackenty J.W., Franx M., 1996, AJ, 111, 1566
- Suchkov, A., Casertano, S., 1997, WFC2 Instrument Science Report 97-01

Figure 1. The surface brightness profiles, and the fits with the PSF-convolved analytical models (for the galaxies for which they could be derived, solid lines).

Figure 2. The effect of the WFPC2 PSF on the deprojected density at  $0.1''$ . For ESO 482G 17, we plot the relative density error  $(\rho_{\text{NO PSF}} - \rho_{\text{PSF}}) / \rho_{\text{PSF}}$  versus the radius of a simulated compact source.  $\rho_{\text{NO PSF}}$  is the density derived by deprojecting the L95 model added of the Plummer-modeled compact source, i.e., is the PSF-free measurement.  $\rho_{\text{PSF}}$  is the density derived by deprojecting the profile obtained from the previous one after convolution with the WFPC2 PSF.

Figure 3. Stellar density profiles obtained by deprojecting the observed surface brightness profiles (dashed lines) and their best fits (solid lines).

Figure 4. Average nuclear slope  $\alpha$  inside  $0.1''$ - $0.5''$  versus absolute F606W magnitude of the spheroidal component. Triangles are the single exponential galaxies, pentagons the double exponential bulges, circles the  $R^{1=4}$ -law bulges, and asterisks the early-type galaxies of L95 and F97 (small symbols) and C97a, C97b (large symbols). Conservative error bars are shown in the upper left corner of the diagram for the galaxies which host a central compact source (large), and for the remaining galaxies (small).

Figure 5. Average nuclear slope inside  $0.1''$ - $0.5''$  ( $\alpha$ ) versus Hubble type (from RC3). Triangles are the single exponential galaxies, pentagons the double exponential bulges, circles the  $R^{1=4}$ -law bulges, and squares the galaxies for which no bulge-component could be fitted.

Figure 6. The L95 fit (dotted line), and the single bulge or bulge plus disk fits (solid line), for four representative galaxies. E482G 17 is fitted with a single exponential, NGC 488 with a single  $R^{1=4}$ -law. For the two-components galaxies (E498G 5, two-exponentials, and NGC 2344,  $R^{1=4}$ -law plus exponential), we plot the bulge (short-dashed line) and disk (long-dashed line) components separately. The total (bulge plus disk) fits and the bulge component overlap at small radii.

Figure 7. Stellar density at  $0.1''$  versus absolute F606W magnitude of the bulge component. Symbols are as in Figure 3. For our sample, they represent the measurements relative to the deprojections of the analytical fits to the surface brightness profiles ( $\rho_{\text{mod},0.1''}$ ). For the galaxies for which the stellar density at  $0.1''$  obtained from the deprojection of the observed surface brightness profile ( $\rho_{\text{data},0.1''}$ ) is significantly larger than  $\rho_{\text{mod},0.1''}$ , an arrow is plotted, which connects the value of  $\rho_{\text{mod},0.1''}$  to the corresponding value of  $\rho_{\text{data},0.1''}$ .

Figure 8. Exponential and  $R^{1.4}$ -law fits performed as a test outside  $1''$ . The results for the same four galaxies of Figure 6 are presented. The solid lines are either a single exponential (left panels) or a double exponential (right panels) fit; the dashed lines are either a single  $R^{1.4}$ -law (left panels) or an  $R^{1.4}$ -law plus exponential (right panels) fit. A no set of two magnitudes has been applied to ESO 482G 17. The kind of profile which provides the bulge classification given in papers I and II still provides a better fit to the inner profiles, even when the innermost  $1''$  is excluded from the fits.

This figure "carolloIII\_fig1a.gif" is available in "gif" format from:

<http://arxiv.org/ps/astro-ph/9804010v1>

This figure "carolloIII\_fig1b.gif" is available in "gif" format from:

<http://arxiv.org/ps/astro-ph/9804010v1>

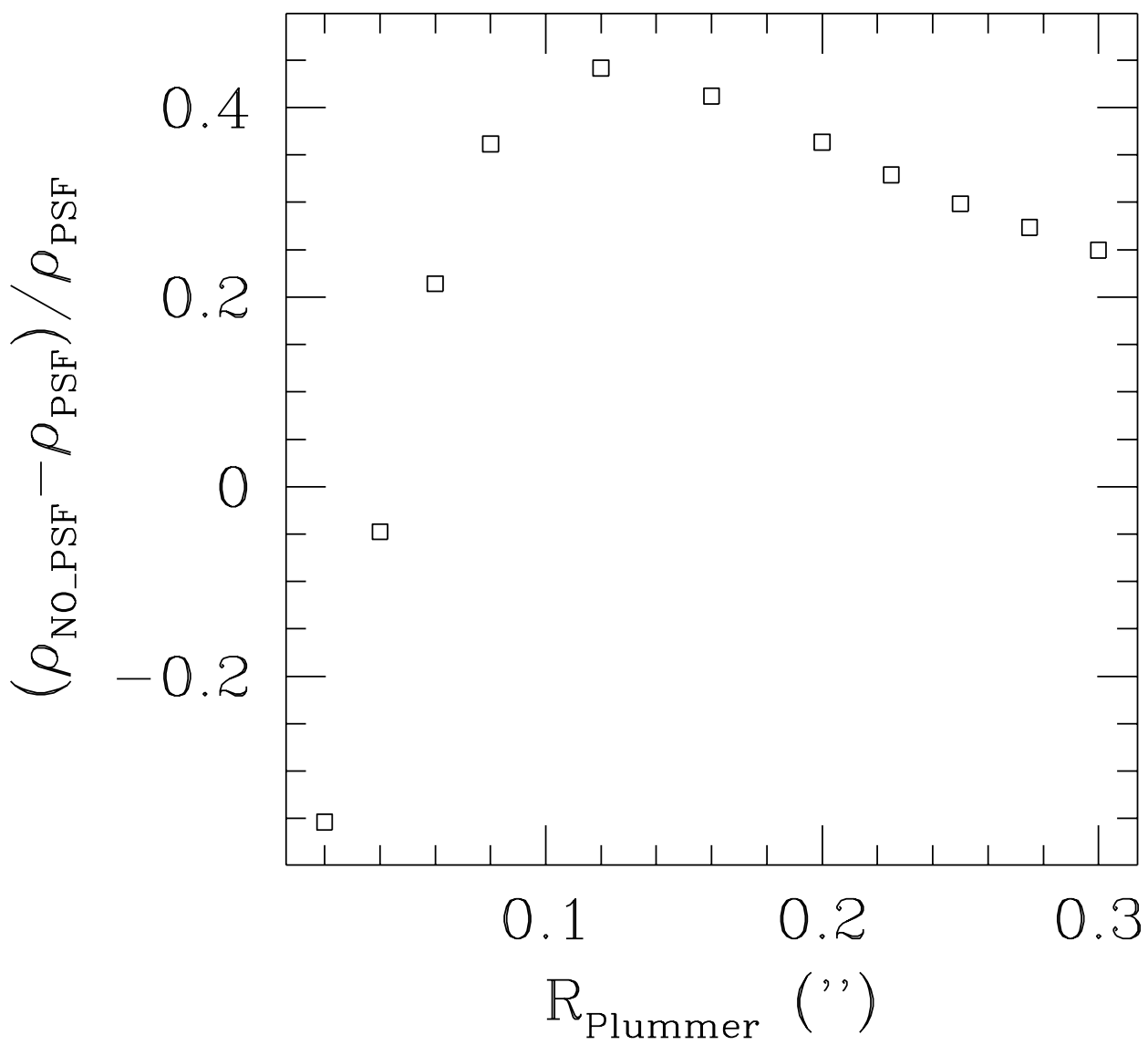
This figure "carolloIII\_fig1c.gif" is available in "gif" format from:

<http://arxiv.org/ps/astro-ph/9804010v1>

This figure "carolloIII\_fig1d.gif" is available in "gif" format from:

<http://arxiv.org/ps/astro-ph/9804010v1>





This figure "carolloIII\_fig3a.gif" is available in "gif" format from:

<http://arxiv.org/ps/astro-ph/9804010v1>

This figure "carolloIII\_fig3b.gif" is available in "gif" format from:

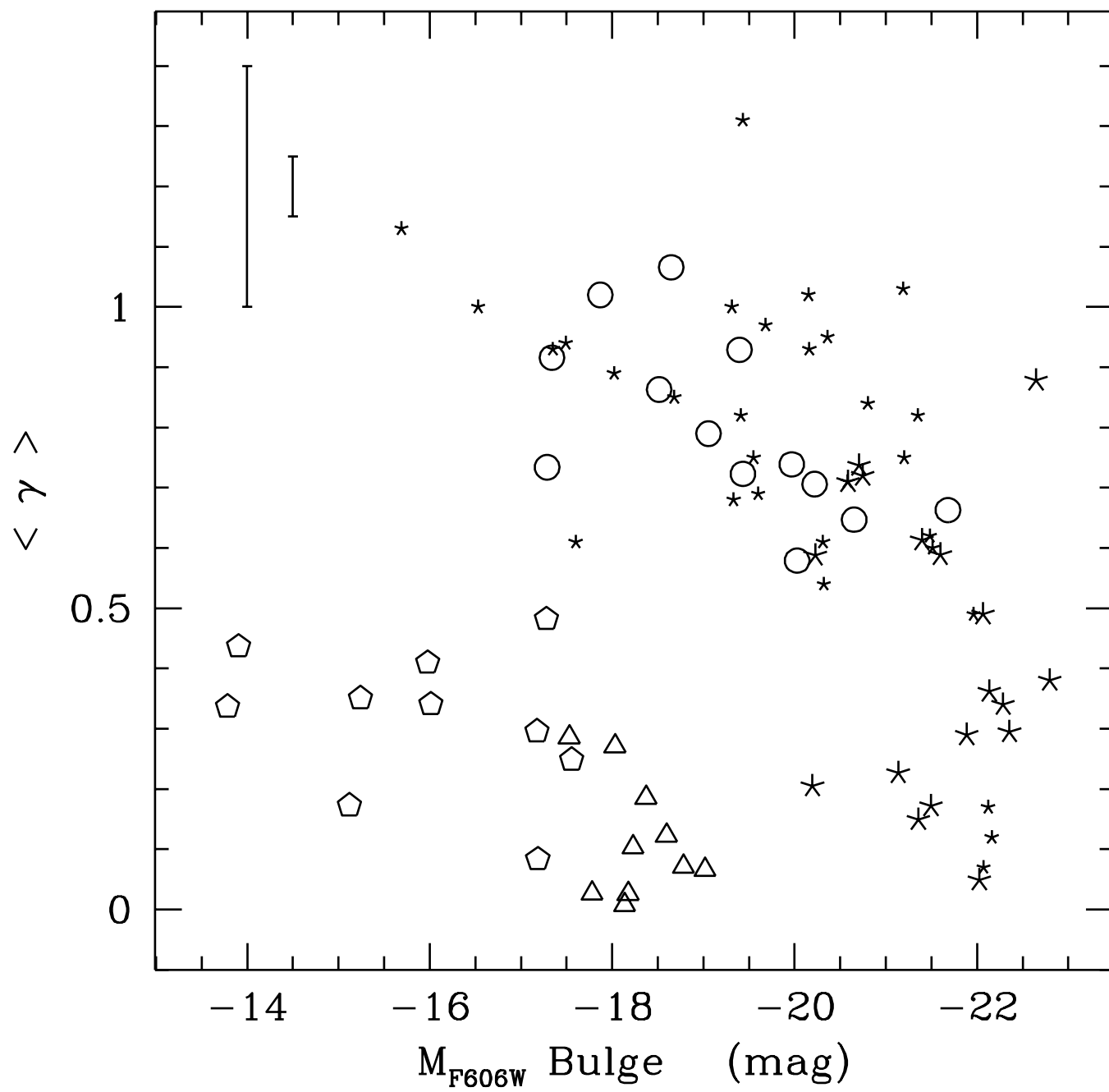
<http://arxiv.org/ps/astro-ph/9804010v1>

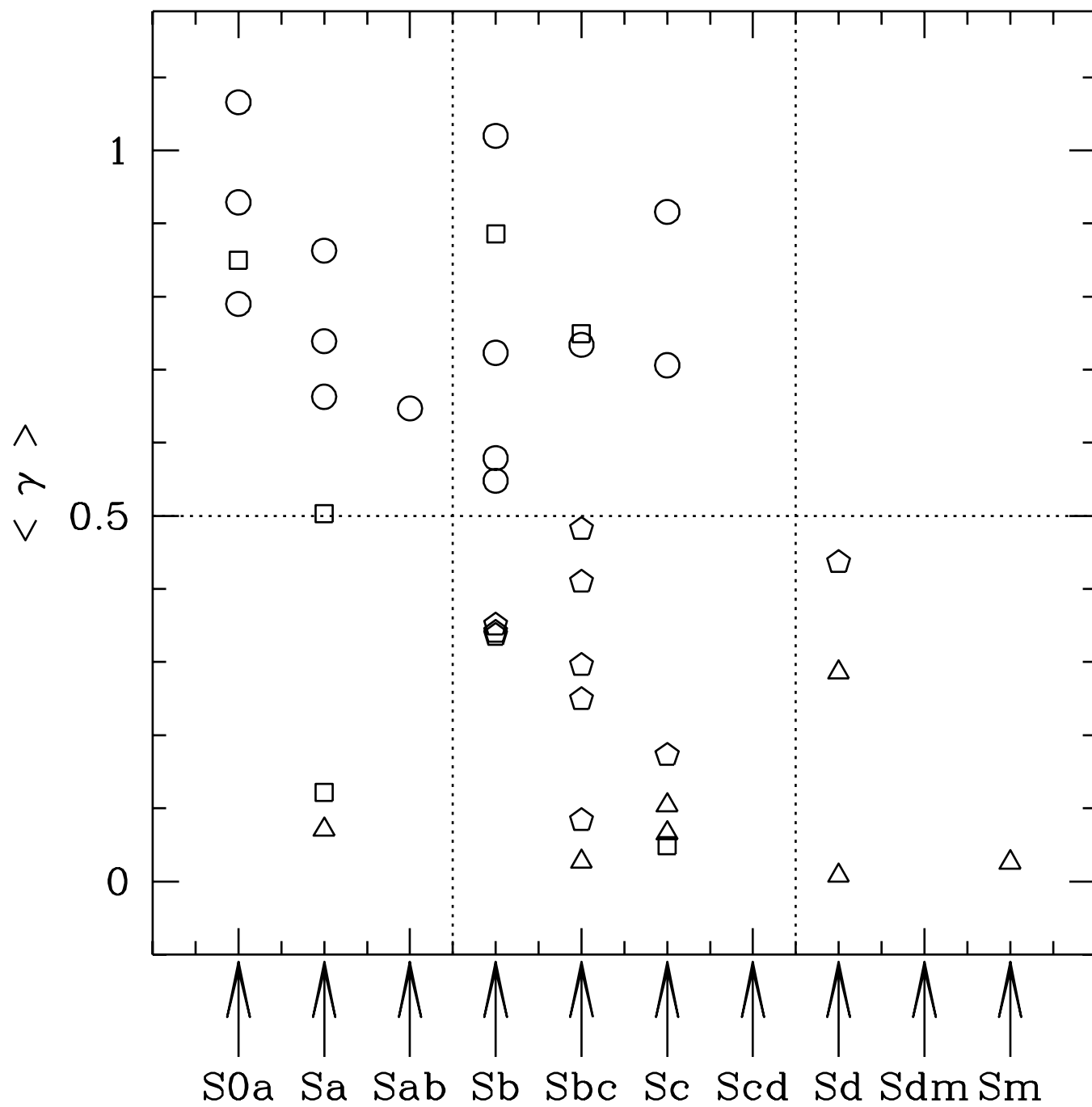
This figure "carolloIII\_fig3c.gif" is available in "gif" format from:

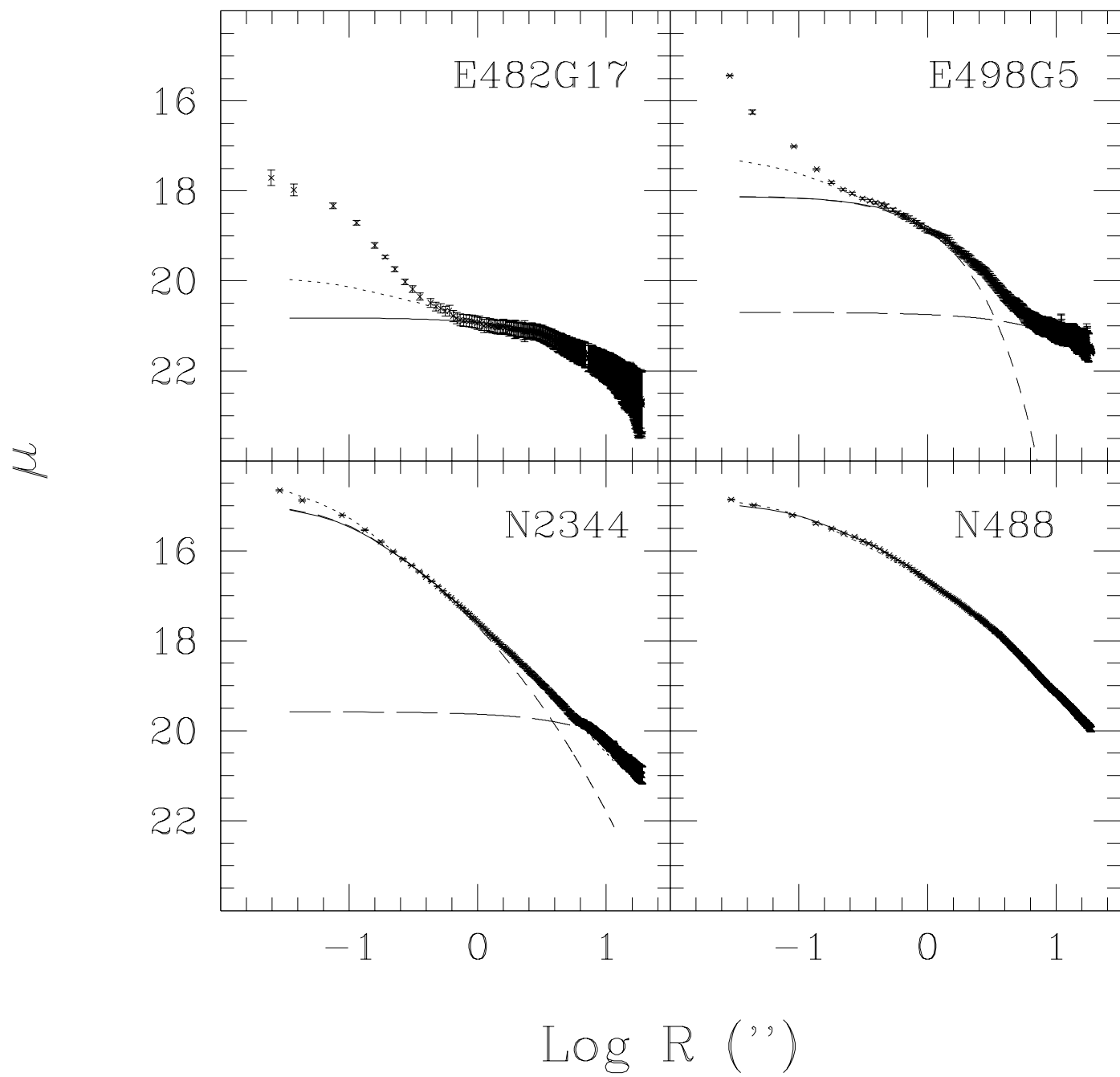
<http://arxiv.org/ps/astro-ph/9804010v1>

This figure "carolloIII\_fig3d.gif" is available in "gif" format from:

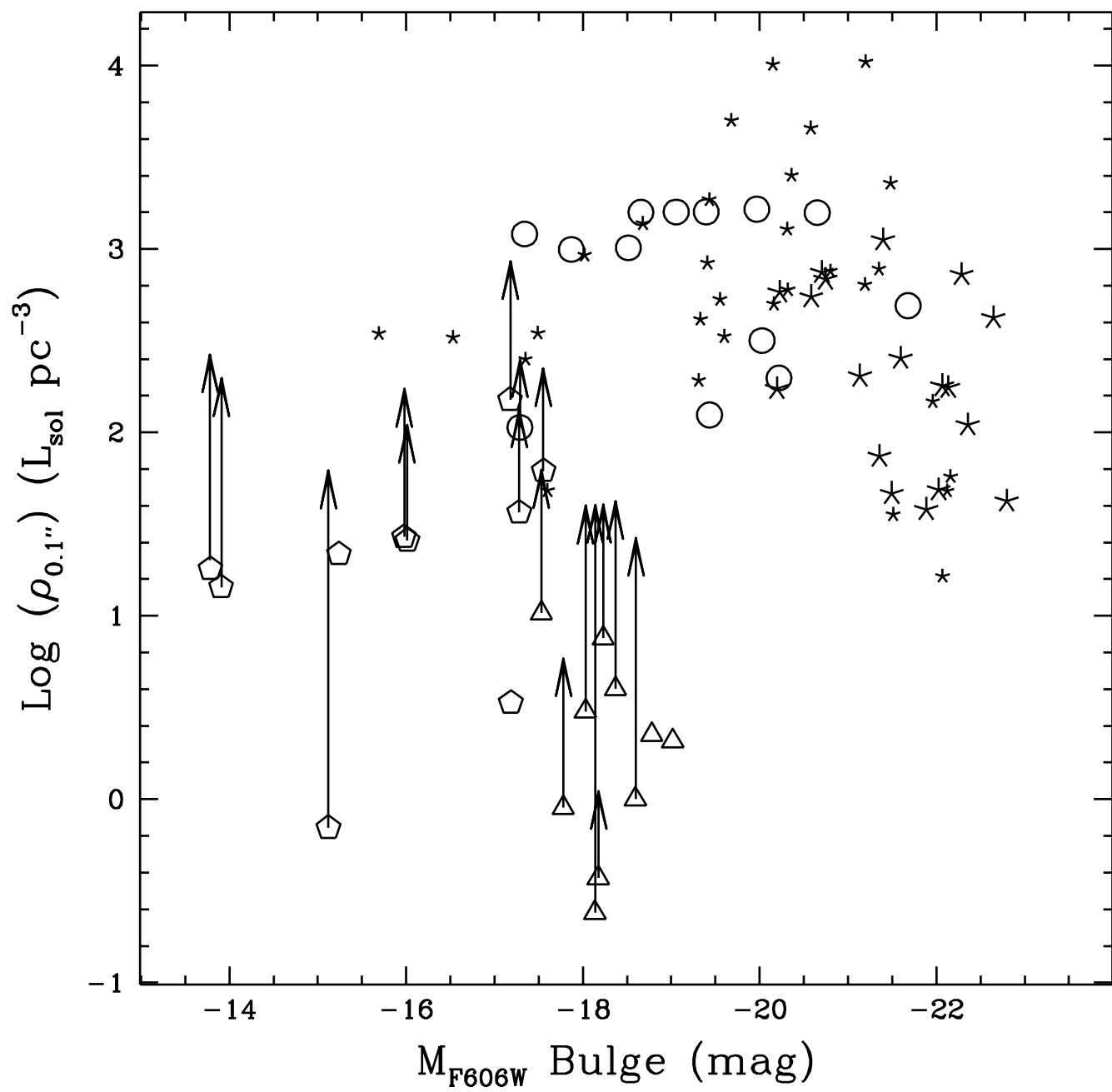
<http://arxiv.org/ps/astro-ph/9804010v1>

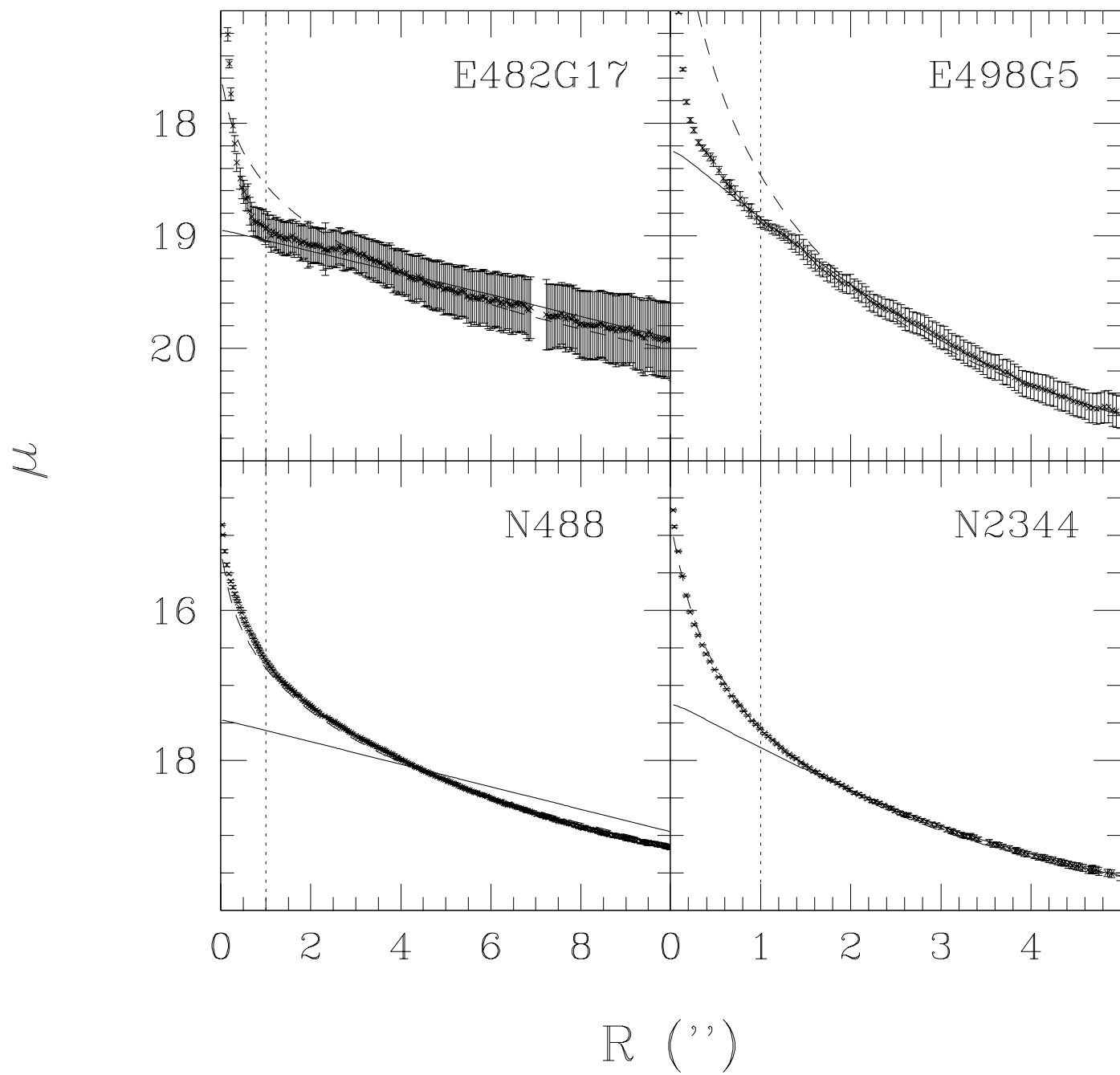












Name	D (M pc)	B (mag)	Type	Compact Source <sup>1</sup>	Bar <sup>2</sup>	Bulge (mag, <sup>00</sup> )
ESO 205 G 7	31	15.02	.SBR 3../Sb	Y	Y	NGF
ESO 240 G 12 <sup>expo1</sup>	28	14.35	.S?....../Sa-b	Y <sup>1</sup>	?	13.64, 9.67
ESO 317 G 20 <sup>R 1=4</sup>	38	12.66	.SAT 5*../Sa	N	N	12.68, 11.83
ESO 482 G 17 <sup>expo1</sup>	24	15.10	.L?....../Sa-b	Y	?	13.87, 16.79
ESO 498 G 5 <sup>expo2</sup>	37	13.81	.SXS4P../Sb	Y	?	15.56, 2.18
ESO 499 G 37 <sup>expo1</sup>	14	13.15	.SXS7*../Sb	Y	?	13.20, 17.52
ESO 508 G 34 <sup>expo1</sup>	30	14.50	.SXS9*../Sb	Y	?	14.21, 9.97
ESO 548 G 10 <sup>expo2</sup>	20	13.30	.SXT 7*../Sb-c	Y	?	17.60, 2.33
ESO 548 G 29 <sup>expo1</sup>	24	14.19	.SB 7/Sb	Y	Y	13.53, 12.13
ESO 549 G 18 <sup>expo2</sup>	24	13.49	.SXT 5../Sb	Y	Y	16.78, 3.75
ESO 572 G 22 <sup>expo1</sup>	27	14.92	.RSB .7P ?/Sb	Y	Y	14.02, 10.41
NGC 406 <sup>expo1</sup>	23	12.88	.SAS5*../Sb	Y	?	12.79, 13.07
NGC 488 <sup>R 1=4</sup>	37	11.15	.SAR 3../S	N	N	10.2, 40.0 (?)
NGC 1325 <sup>expo2</sup>	27	12.30	.SA S4../Sd	Y	N	16.18, 1.85
NGC 1345 <sup>expo1</sup>	24	13.57	.SB S5P*/SB a	Y	Y	13.67, 5.89
NGC 1483 <sup>expo1</sup>	16	13.23	.SB S4*../Sb-c	Y <sup>1</sup>	Y	13.24, 13.33
NGC 1640 <sup>R 1=4</sup>	25	12.48	.SBR 3../S(r)a	N	ETB	14.12, 2.47
NGC 2082 <sup>expo2</sup>	19	12.64	.SBR 3../Sb	Y	Y	15.38, 3.70
NGC 2196 <sup>R 1=4</sup>	35	11.66	.PSA S1../Sa	N	N	11.04, 22.94
NGC 2344 <sup>R 1=4</sup>	14	12.68	.SAT 5*../Sb	N	N	13.39, 6.18
NGC 2460 <sup>R 1=4</sup>	26	12.38	.SA S1../Sb	N	N	13.56, 3.93
NGC 2758 <sup>expo2</sup>	30	13.46	.PSB .4P ?/Sb:	Y	?	15.20, 2.81
NGC 3045 <sup>expo2</sup>	35	13.61	.SAR 3?../Sb	N	?	17.48, 0.86
NGC 3054 <sup>R 1=4</sup>	34	11.95	.SXR 3../Sb	N	ETB	12.63, 9.31
NGC 3177 <sup>expo2</sup>	19	13.07	.SAT 3../Sb	Y	N	15.58, 0.42
NGC 3259 <sup>R 1=4</sup>	27	12.97	.SXT 4*../Sb	Y <sup>1</sup>	N	14.87, 7.44
NGC 3277	22	12.55	.SAR 2../Sa-Sb	N	N	NGF
NGC 3455 <sup>expo2</sup>	19	12.87	.PSXT 3../Sb	Y	?	17.61, 1.53
NGC 3898 <sup>R 1=4</sup>	22	11.63	.SA S2../Sa	N	N	11.06, 11.74
NGC 3900 <sup>R 1=4</sup>	27	12.30	.LAR + ../Sa	Y	N	13.50, 2.85
NGC 3928	17	12.94	.E?....../-	Y	N	NGF
NGC 4030 <sup>expo2</sup>	20	11.37	.SA S4../Sb	Y	N	14.33, 2.0
NGC 4260	29	12.61	.SB S1../SB a	N	ETB	NGF
NGC 4384	37	13.54	.S..I../Sa	Y	?	NGF
NGC 4806	37	13.09	.SB S5?../Sb	Y	N	NGF
NGC 4980 <sup>expo1</sup>	22	13.19	.SXT 1P ?/Sa	Y	?	12.93, 12.81
NGC 5121 <sup>R 1=4</sup>	23	11.27	.PSA S1../Sa	N	N	11.84, 7.10
NGC 5985 <sup>R 1=4</sup>	46	11.67	.SXR 3../Sb	N	ETB?	13.88, 8.0
NGC 6340 <sup>R 1=4</sup>	18	11.82	.SA S0../Sa	N	N	12.22, 8.03
NGC 6384 <sup>expo2</sup>	26	11.29	.SXR 4../Sb	Y	Y	14.52, 1.95
NGC 7280 <sup>R 1=4</sup>	28	13.00	.LXR + ../S0-Sa	N	N	12.84, 3.51
NGC 7421	26	12.62	.SB T 4../Sb-c	Y	Y	NGF
NGC 7690	21	13.03	.SAR 3*\$../Sb	Y	N	NGF

Table 1: Parameters for the 43 galaxies. Distance  $D$  and total  $B$  magnitude are from the RC3 catalogue (de Vaucouleurs et al. 1991). Morphological type is from the ESO LV (Lauberts & Valentijn 1989) or UGC (Nilson 1971) catalogues (left), or from the RC3 catalogue (right). The information provided in the other columns is extracted from papers I and II. | A "\Y" indicates the presence of a central compact source, a "\N" stands for no central compact source.<sup>1</sup> The central source in ESO 240 G 12, NGC 1483 and NGC 3259 is unresolved. ~ A "\Y" indicates the presence of a bar, a "\N" stands for no barred component. A question mark indicates that a faint bar might be present, or that the entire galaxy has a flattened, bar-like (irregular) morphology. \ETB" indicates the presence of an early-type bar. The column lists the total apparent magnitude in F606W and the half-light radius  $R_e$  (in <sup>00</sup>) of the bulges. Close to the galaxy name, the superscript  $R^{1=4}$ , expo1 or expo2 identifies galaxies whose bulge-like component has been fitted with a  $R^{1=4}$ -law or an (single or double) exponential profile. All magnitudes are corrected for Galactic extinction using the values published by Burstein & Heiles (1984).

Nam e	Range ( <sup>00</sup> )				R <sub>b</sub> ( <sup>00</sup> )	b (m ag)	h i
ESO 205 G 7	-	-	-	-	-	-	-
ESO 240 G 12	0.16-10	1.362	1.799	0.182	6.506	20.70	0.188
	0.7-10	1.147	1.560	0.000	4.190	20.29	0.058
ESO 317 G 20	0-10	4.850	0.937	0.498	0.220	16.17	0.706
ESO 482 G 17	0.3-10	70.40	0.596	0.290	3.669	21.26	0.271
ESO 498 G 5	0.16-10	5.582	1.007	0.522	1.052	18.87	0.482
ESO 499 G 37	0.7-10	5.548	0.823	0.306	5.101	20.80	0.286
ESO 508 G 34	0-10	1.497	1.599	0.000	4.021	20.85	0.026
ESO 548 G 10	0.3-10	19.22	0.704	0.459	3.548	20.82	0.437
ESO 548 G 29		3.0	0.90	0.20	3.50	20.86	0.186
ESO 549 G 18	0.16-10	5.167	0.682	0.360	3.666	20.86	0.339
	0.7-10	1.231	0.819	0.008	2.153	20.59	0.006
ESO 572 G 22	0.16-10	1.945	1.413	0.000	3.763	20.62	0.008
NGC 406	0.2-10	3.963	1.315	0.072	4.645	19.82	0.066
NGC 488	0-10	0.643	2.148	0.419	8.817	19.01	0.548
NGC 1325	0.16-10	0.302	0.975	0.208	1.050	18.88	0.480
	0.25-10	3.359	0.674	0.343	0.690	18.59	0.340
NGC 1345	0.3-10	6.973	1.454	0.113	2.026	18.83	0.104
NGC 1483	0.3-10	1.365	1.060	0.000	3.724	20.28	0.027
NGC 1640	0-10	59.85	1.024	0.895	0.020	13.05	1.020
NGC 2082	0.16-10	20.74	0.652	0.345	2.511	19.42	0.324
	0.7-10	49.17	0.654	0.378	2.680	19.50	0.357
NGC 2196		2.979	1.195	0.695	1.702	17.21	0.663
NGC 2344	0-5	0.415	1.435	0.694	1.177	17.77	0.916
NGC 2460	0-10	5.180	1.726	0.926	8.300	19.26	0.913
	0.2-7	1.942	0.990	0.827	1.042	17.03	0.813
NGC 2758	0.3-10	1.756	1.318	0.000	1.515	18.78	0.060
	0.16-10	1.319	1.452	0.000	1.703	18.88	0.107
NGC 3045	0.11-5	70.34	0.590	0.370	0.551	18.51	0.351
NGC 3054	0-10	6.382	1.179	0.553	0.441	16.26	0.579
NGC 3177	-	-	-	-	-	-	-
NGC 3259	0.3-5	0.156	0.441	1.026	0.120	17.07	0.690
	0.3-10	0.214	0.040	1.292	1.445	18.98	0.777
NGC 3277	0-10	54.61	1.140	0.869	0.594	16.21	0.850
NGC 3455	0.3-10	0.443	0.621	0.299	3.583	20.08	0.351
	0.2-5	0.536	0.734	0.251	3.422	20.07	0.323
NGC 3898	0-10	0.916	1.499	0.304	0.553	15.29	0.647
NGC 3900	0-10	0.123	1.613	0.600	0.565	16.28	1.078
	0.2-10	0.099	2.011	0.252	1.535	17.43	1.054
NGC 3928	0.3-10	87.84	1.767	0.657	2.431	17.98	0.620
NGC 4030	0.3-10	93.68	0.759	0.316	1.059	16.98	0.296
NGC 4260	0-10	0.365	2.426	0.000	7.464	19.57	0.503
NGC 4384	0-10	1.960	1.099	0.000	0.764	18.11	0.122
NGC 4806		1.673	0.629	0.000	1.138	19.36	0.049
NGC 4980	0-10	379.0	0.669	0.077	2.965	19.67	0.071
NGC 5121	0-10	56.22	1.408	.799	0.886	15.88	0.772
		13.52	1.402	0.738	0.819	15.86	0.706
NGC 5985	0.1-10	41.85	1.046	0.754	2.346	18.78	0.723
NGC 6340	0-10	1.728	1.238	0.716	0.538	15.98	0.790
NGC 6384	0.3-10	0.843	1.696	0.000	1.803	17.78	0.249
NGC 7280	0.2-10	73.65	1.472	0.914	0.772	16.16	0.900
	0-10	15.42	1.472	0.965	0.802	16.24	0.958
NGC 7421	0.3-10	1.677	1.098	0.743	2.720	19.02	0.718
	0.2-10	9.315	1.012	0.806	2.490	18.92	0.779
NGC 7690	0-10	144.8	1.965	0.902	4.534	18.57	0.886

Table 2: The best  $\chi^2$  values for  $R_b$ ,  $\alpha$ ,  $\beta$ ,  $\gamma$ ,  $\delta$ ,  $\epsilon$ ,  $\zeta$ ,  $\eta$ ,  $\theta$ ,  $\iota$ ,  $\kappa$ ,  $\lambda$ ,  $\mu$ ,  $\nu$ ,  $\xi$ ,  $\omicron$ ,  $\pi$ ,  $\rho$ ,  $\sigma$ ,  $\tau$ ,  $\upsilon$ ,  $\phi$ ,  $\chi$ ,  $\psi$ ,  $\omega$ ,  $\delta$ ,  $\epsilon$ ,  $\zeta$ ,  $\eta$ ,  $\theta$ ,  $\iota$ ,  $\kappa$ ,  $\lambda$ ,  $\mu$ ,  $\nu$ ,  $\xi$ ,  $\omicron$ ,  $\pi$ ,  $\rho$ ,  $\sigma$ ,  $\tau$ ,  $\upsilon$ ,  $\phi$ ,  $\chi$ ,  $\psi$ ,  $\omega$ ,  $\delta$ ,  $\epsilon$ ,  $\zeta$ ,  $\eta$ ,  $\theta$ ,  $\iota$ ,  $\kappa$ ,  $\lambda$ ,  $\mu$ ,  $\nu$ ,  $\xi$ ,  $\omicron$ ,  $\pi$ ,  $\rho$ ,  $\sigma$ ,  $\tau$ ,  $\upsilon$ ,  $\phi$ ,  $\chi$ ,  $\psi$ ,  $\omega$ ,  $\delta$ ,  $\epsilon$ ,  $\zeta$ ,  $\eta$ ,  $\theta$ ,  $\iota$ ,  $\kappa$ ,  $\lambda$ ,  $\mu$ ,  $\nu$ ,  $\xi$ ,  $\omicron$ ,  $\pi$ ,  $\rho$ ,  $\sigma$ ,  $\tau$ ,  $\upsilon$ ,  $\phi$ ,  $\chi$ ,  $\psi$ ,  $\omega$ ,  $\delta$ ,  $\epsilon$ ,  $\zeta$ ,  $\eta$ ,  $\theta$ ,  $\iota$ ,  $\kappa$ ,  $\lambda$ ,  $\mu$ ,  $\nu$ ,  $\xi$ ,  $\omicron$ ,  $\pi$ ,  $\rho$ ,  $\sigma$ ,  $\tau$ ,  $\upsilon$ ,  $\phi$ ,  $\chi$ ,  $\psi$ ,  $\omega$ ,  $\delta$ ,  $\epsilon$ ,  $\zeta$ ,  $\eta$ ,  $\theta$ ,  $\iota$ ,  $\kappa$ ,  $\lambda$ ,  $\mu$ ,  $\nu$ ,  $\xi$ ,  $\omicron$ ,  $\pi$ ,  $\rho$ ,  $\sigma$ ,  $\tau$ ,  $\upsilon$ ,  $\phi$ ,  $\chi$ ,  $\psi$ ,  $\omega$ ,  $\delta$ ,  $\epsilon$ ,  $\zeta$ ,  $\eta$ ,  $\theta$ ,  $\iota$ ,  $\kappa$ ,  $\lambda$ ,  $\mu$ ,  $\nu$ ,  $\xi$ ,  $\omicron$ ,  $\pi$ ,  $\rho$ ,  $\sigma$ ,  $\tau$ ,  $\upsilon$ ,  $\phi$ ,  $\chi$ ,  $\psi$ ,  $\omega$ ,  $\delta$ ,  $\epsilon$ ,  $\zeta$ ,  $\eta$ ,  $\theta$ ,  $\iota$ ,  $\kappa$ ,  $\lambda$ ,  $\mu$ ,  $\nu$ ,  $\xi$ ,  $\omicron$ ,  $\pi$ ,  $\rho$ ,  $\sigma$ ,  $\tau$ ,  $\upsilon$ ,  $\phi$ ,  $\chi$ ,  $\psi$ ,  $\omega$ ,  $\delta$ ,  $\epsilon$ ,  $\zeta$ ,  $\eta$ ,  $\theta$ ,  $\iota$ ,  $\kappa$ ,  $\lambda$ ,  $\mu$ ,  $\nu$ ,  $\xi$ ,  $\omicron$ ,  $\pi$ ,  $\rho$ ,  $\sigma$ ,  $\tau$ ,  $\upsilon$ ,  $\phi$ ,  $\chi$ ,  $\psi$ ,  $\omega$ ,  $\delta$ ,  $\epsilon$ ,  $\zeta$ ,  $\eta$ ,  $\theta$ ,  $\iota$ ,  $\kappa$ ,  $\lambda$ ,  $\mu$ ,  $\nu$ ,  $\xi$ ,  $\omicron$ ,  $\pi$ ,  $\rho$ ,  $\sigma$ ,  $\tau$ ,  $\upsilon$ ,  $\phi$ ,  $\chi$ ,  $\psi$ ,  $\omega$ ,  $\delta$ ,  $\epsilon$ ,  $\zeta$ ,  $\eta$ ,  $\theta$ ,  $\iota$ ,  $\kappa$ ,  $\lambda$ ,  $\mu$ ,  $\nu$ ,  $\xi$ ,  $\omicron$ ,  $\pi$ ,  $\rho$ ,  $\sigma$ ,  $\tau$ ,  $\upsilon$ ,  $\phi$ ,  $\chi$ ,  $\psi$ ,  $\omega$ ,  $\delta$ ,  $\epsilon$ ,  $\zeta$ ,  $\eta$ ,  $\theta$ ,  $\iota$ ,  $\kappa$ ,  $\lambda$ ,  $\mu$ ,  $\nu$ ,  $\xi$ ,  $\omicron$ ,  $\pi$ ,  $\rho$ ,  $\sigma$ ,  $\tau$ ,  $\upsilon$ ,  $\phi$ ,  $\chi$ ,  $\psi$ ,  $\omega$ ,  $\delta$ ,  $\epsilon$ ,  $\zeta$ ,  $\eta$ ,  $\theta$ ,  $\iota$ ,  $\kappa$ ,  $\lambda$ ,  $\mu$ ,  $\nu$ ,  $\xi$ ,  $\omicron$ ,  $\pi$ ,  $\rho$ ,  $\sigma$ ,  $\tau$ ,  $\upsilon$ ,  $\phi$ ,  $\chi$ ,  $\psi$ ,  $\omega$ ,  $\delta$ ,  $\epsilon$ ,  $\zeta$ ,  $\eta$ ,  $\theta$ ,  $\iota$ ,  $\kappa$ ,  $\lambda$ ,  $\mu$ ,  $\nu$ ,  $\xi$ ,  $\omicron$ ,  $\pi$ ,  $\rho$ ,  $\sigma$ ,  $\tau$ ,  $\upsilon$ ,  $\phi$ ,  $\chi$ ,  $\psi$ ,  $\omega$ ,  $\delta$ ,  $\epsilon$ ,  $\zeta$ ,  $\eta$ ,  $\theta$ ,  $\iota$ ,  $\kappa$ ,  $\lambda$ ,  $\mu$ ,  $\nu$ ,  $\xi$ ,  $\omicron$ ,  $\pi$ ,  $\rho$ ,  $\sigma$ ,  $\tau$ ,  $\upsilon$ ,  $\phi$ ,  $\chi$ ,  $\psi$ ,  $\omega$ ,  $\delta$ ,  $\epsilon$ ,  $\zeta$ ,  $\eta$ ,  $\theta$ ,  $\iota$ ,  $\kappa$ ,  $\lambda$ ,  $\mu$ ,  $\nu$ ,  $\xi$ ,  $\omicron$ ,  $\pi$ ,  $\rho$ ,  $\sigma$ ,  $\tau$ ,  $\upsilon$ ,  $\phi$ ,  $\chi$ ,  $\psi$ ,  $\omega$ ,  $\delta$ ,  $\epsilon$ ,  $\zeta$ ,  $\eta$ ,  $\theta$ ,  $\iota$ ,  $\kappa$ ,  $\lambda$ ,  $\mu$ ,  $\nu$ ,  $\xi$ ,  $\omicron$ ,  $\pi$ ,  $\rho$ ,  $\sigma$ ,  $\tau$ ,  $\upsilon$ ,  $\phi$ ,  $\chi$ ,  $\psi$ ,  $\omega$ ,  $\delta$ ,  $\epsilon$ ,  $\zeta$ ,  $\eta$ ,  $\theta$ ,  $\iota$ ,  $\kappa$ ,  $\lambda$ ,  $\mu$ ,  $\nu$ ,  $\xi$ ,  $\omicron$ ,  $\pi$ ,  $\rho$ ,  $\sigma$ ,  $\tau$ ,  $\upsilon$ ,  $\phi$ ,  $\chi$ ,  $\psi$ ,  $\omega$ ,  $\delta$ ,  $\epsilon$ ,  $\zeta$ ,  $\eta$ ,  $\theta$ ,  $\iota$ ,  $\kappa$ ,  $\lambda$ ,  $\mu$ ,  $\nu$ ,  $\xi$ ,  $\omicron$ ,  $\pi$ ,  $\rho$ ,  $\sigma$ ,  $\tau$ ,  $\upsilon$ ,  $\phi$ ,  $\chi$ ,  $\psi$ ,  $\omega$ ,  $\delta$ ,  $\epsilon$ ,  $\zeta$ ,  $\eta$ ,  $\theta$ ,  $\iota$ ,  $\kappa$ ,  $\lambda$ ,  $\mu$ ,  $\nu$ ,  $\xi$ ,  $\omicron$ ,  $\pi$ ,  $\rho$ ,  $\sigma$ ,  $\tau$ ,  $\upsilon$ ,  $\phi$ ,  $\chi$ ,  $\psi$ ,  $\omega$ ,  $\delta$ ,  $\epsilon$ ,  $\zeta$ ,  $\eta$ ,  $\theta$ ,  $\iota$ ,  $\kappa$ ,  $\lambda$ ,  $\mu$ ,  $\nu$ ,  $\xi$ ,  $\omicron$ ,  $\pi$ ,  $\rho$ ,  $\sigma$ ,  $\tau$ ,  $\upsilon$ ,  $\phi$ ,  $\chi$ ,  $\psi$ ,  $\omega$ ,  $\delta$ ,  $\epsilon$ ,  $\zeta$ ,  $\eta$ ,  $\theta$ ,  $\iota$ ,  $\kappa$ ,  $\lambda$ ,  $\mu$ ,  $\nu$ ,  $\xi$ ,  $\omicron$ ,  $\pi$ ,  $\rho$ ,  $\sigma$ ,  $\tau$ ,  $\upsilon$ ,  $\phi$ ,  $\chi$ ,  $\psi$ ,  $\omega$ ,  $\delta$ ,  $\epsilon$ ,  $\zeta$ ,  $\eta$ ,  $\theta$ ,  $\iota$ ,  $\kappa$ ,  $\lambda$ ,  $\mu$ ,  $\nu$ ,  $\xi$ ,  $\omicron$ ,  $\pi$ ,  $\rho$ ,  $\sigma$ ,  $\tau$ ,  $\upsilon$ ,  $\phi$ ,  $\chi$ ,  $\psi$ ,  $\omega$ ,  $\delta$ ,  $\epsilon$ ,  $\zeta$ ,  $\eta$ ,  $\theta$ ,  $\iota$ ,  $\kappa$ ,  $\lambda$ ,  $\mu$ ,  $\nu$ ,  $\xi$ ,  $\omicron$ ,  $\pi$ ,  $\rho$ ,  $\sigma$ ,  $\tau$ ,  $\upsilon$ ,  $\phi$ ,  $\chi$ ,  $\psi$ ,  $\omega$ ,  $\delta$ ,  $\epsilon$ ,  $\zeta$ ,  $\eta$ ,  $\theta$ ,  $\iota$ ,  $\kappa$ ,  $\lambda$ ,  $\mu$ ,  $\nu$ ,  $\xi$ ,  $\omicron$ ,  $\pi$ ,  $\rho$ ,  $\sigma$ ,  $\tau$ ,  $\upsilon$ ,  $\phi$ ,  $\chi$ ,  $\psi$ ,  $\omega$ ,  $\delta$ ,  $\epsilon$ ,  $\zeta$ ,  $\eta$ ,  $\theta$ ,  $\iota$ ,  $\kappa$ ,  $\lambda$ ,  $\mu$ ,  $\nu$ ,  $\xi$ ,  $\omicron$ ,  $\pi$ ,  $\rho$ ,  $\sigma$ ,  $\tau$ ,  $\upsilon$ ,  $\phi$ ,  $\chi$ ,  $\psi$ ,  $\omega$ ,  $\delta$ ,  $\epsilon$ ,  $\zeta$ ,  $\eta$ ,  $\theta$ ,  $\iota$ ,  $\kappa$ ,  $\lambda$ ,  $\mu$ ,  $\nu$ ,  $\xi$ ,  $\omicron$ ,  $\pi$ ,  $\rho$ ,  $\sigma$ ,  $\tau$ ,  $\upsilon$ ,  $\phi$ ,  $\chi$ ,  $\psi$ ,  $\omega$ ,  $\delta$ ,  $\epsilon$ ,  $\zeta$ ,  $\eta$ ,  $\theta$ ,  $\iota$ ,  $\kappa$ ,  $\lambda$ ,  $\mu$ ,  $\nu$ ,  $\xi$ ,  $\omicron$ ,  $\pi$ ,  $\rho$ ,  $\sigma$ ,  $\tau$ ,  $\upsilon$ ,  $\phi$ ,  $\chi$ ,  $\psi$ ,  $\omega$ ,  $\delta$ ,  $\epsilon$ ,  $\zeta$ ,  $\eta$ ,  $\theta$ ,  $\iota$ ,  $\kappa$ ,  $\lambda$ ,  $\mu$ ,  $\nu$ ,  $\xi$ ,  $\omicron$ ,  $\pi$ ,  $\rho$ ,  $\sigma$ ,  $\tau$ ,  $\upsilon$ ,  $\phi$ ,  $\chi$ ,  $\psi$ ,  $\omega$ ,  $\delta$ ,  $\epsilon$ ,  $\zeta$ ,  $\eta$ ,  $\theta$ ,  $\iota$ ,  $\kappa$ ,  $\lambda$ ,  $\mu$ ,  $\nu$ ,  $\xi$ ,  $\omicron$ ,  $\pi$ ,  $\rho$ ,  $\sigma$ ,  $\tau$ ,  $\upsilon$ ,  $\phi$ ,  $\chi$ ,  $\psi$ ,  $\omega$ ,  $\delta$ ,  $\epsilon$ ,  $\zeta$ ,  $\eta$ ,  $\theta$ ,  $\iota$ ,  $\kappa$ ,  $\lambda$ ,  $\mu$ ,  $\nu$ ,  $\xi$ ,  $\omicron$ ,  $\pi$ ,  $\rho$ ,  $\sigma$ ,  $\tau$ ,  $\upsilon$ ,  $\phi$ ,  $\chi$ ,  $\psi$ ,  $\omega$ ,  $\delta$ ,  $\epsilon$ ,  $\zeta$ ,  $\eta$ ,  $\theta$ ,  $\iota$ ,  $\kappa$ ,  $\lambda$ ,  $\mu$ ,  $\nu$ ,  $\xi$ ,  $\omicron$ ,  $\pi$ ,  $\rho$ ,  $\sigma$ ,  $\tau$ ,  $\upsilon$ ,  $\phi$ ,  $\chi$ ,  $\psi$ ,  $\omega$ ,  $\delta$ ,  $\epsilon$ ,  $\zeta$ ,  $\eta$ ,  $\theta$ ,  $\iota$ ,  $\kappa$ ,  $\lambda$ ,  $\mu$ ,  $\nu$ ,  $\xi$ ,  $\omicron$ ,  $\pi$ ,  $\rho$ ,  $\sigma$ ,  $\tau$ ,  $\upsilon$ ,  $\phi$ ,  $\chi$ ,  $\psi$ ,  $\omega$ ,  $\delta$ ,  $\epsilon$ ,  $\zeta$ ,  $\eta$ ,  $\theta$ ,  $\iota$ ,  $\kappa$ ,  $\lambda$ ,  $\mu$ ,  $\nu$ ,  $\xi$ ,  $\omicron$ ,  $\pi$ ,  $\rho$ ,  $\sigma$ ,  $\tau$ ,  $\upsilon$ ,  $\phi$ ,  $\chi$ ,  $\psi$ ,  $\omega$ ,  $\delta$ ,  $\epsilon$ ,  $\zeta$ ,  $\eta$ ,  $\theta$ ,  $\iota$ ,  $\kappa$ ,  $\lambda$ ,  $\mu$ ,  $\nu$ ,  $\xi$ ,  $\omicron$ ,  $\pi$ ,  $\rho$ ,  $\sigma$ ,  $\tau$ ,  $\upsilon$ ,  $\phi$ ,  $\chi$ ,  $\psi$ ,  $\omega$ ,  $\delta$ ,  $\epsilon$ ,  $\zeta$ ,  $\eta$ ,  $\theta$ ,  $\iota$ ,  $\kappa$ ,  $\lambda$ ,  $\mu$ ,  $\nu$ ,  $\xi$ ,  $\omicron$ ,  $\pi$ ,  $\rho$ ,  $\sigma$ ,  $\tau$ ,  $\upsilon$ ,  $\phi$ ,  $\chi$ ,  $\psi$ ,  $\omega$ ,  $\delta$ ,  $\epsilon$ ,  $\zeta$ ,  $\eta$ ,  $\theta$ ,  $\iota$ ,  $\kappa$ ,  $\lambda$ ,  $\mu$ ,  $\nu$ ,  $\xi$ ,  $\omicron$ ,  $\pi$ ,  $\rho$ ,  $\sigma$ ,  $\tau$ ,  $\upsilon$ ,  $\phi$ ,  $\chi$ ,  $\psi$ ,  $\omega$ ,  $\delta$ ,  $\epsilon$ ,  $\zeta$ ,  $\eta$ ,  $\theta$ ,  $\iota$ ,  $\kappa$ ,  $\lambda$ ,  $\mu$ ,  $\nu$ ,  $\xi$ ,  $\omicron$ ,  $\pi$ ,  $\rho$ ,  $\sigma$ ,  $\tau$ ,  $\upsilon$ ,  $\phi$ ,  $\chi$ ,  $\psi$ ,  $\omega$ ,  $\delta$ ,  $\epsilon$ ,  $\zeta$ ,  $\eta$ ,  $\theta$ ,  $\iota$ ,  $\kappa$ ,  $\lambda$ ,  $\mu$ ,  $\nu$ ,  $\xi$ ,  $\omicron$ ,  $\pi$ ,  $\rho$ ,  $\sigma$ ,  $\tau$ ,  $\upsilon$ ,  $\phi$ ,  $\chi$ ,  $\psi$ ,  $\omega$ ,  $\delta$ ,  $\epsilon$ ,  $\zeta$ ,  $\eta$ ,  $\theta$ ,  $\iota$ ,  $\kappa$ ,  $\lambda$ ,  $\mu$ ,  $\nu$ ,  $\xi$ ,  $\omicron$ ,  $\pi$ ,  $\rho$ ,  $\sigma$ ,  $\tau$ ,  $\upsilon$ ,  $\phi$ ,  $\chi$ ,  $\psi$ ,  $\omega$ ,  $\delta$ ,  $\epsilon$ ,  $\zeta$ ,  $\eta$ ,  $\theta$ ,  $\iota$ ,  $\kappa$ ,  $\lambda$ ,  $\mu$ ,  $\nu$ ,  $\xi$ ,  $\omicron$ ,  $\pi$ ,  $\rho$ ,  $\sigma$ ,  $\tau$ ,  $\upsilon$ ,  $\phi$ ,  $\chi$ ,  $\psi$ ,  $\omega$ ,  $\delta$ ,  $\epsilon$ ,  $\zeta$ ,  $\eta$ ,  $\theta$ ,  $\iota$ ,  $\kappa$ ,  $\lambda$ ,  $\mu$ ,  $\nu$ ,  $\xi$ ,  $\omicron$ ,  $\pi$ ,  $\rho$ ,  $\sigma$ ,  $\tau$ ,  $\upsilon$ ,  $\phi$ ,  $\chi$ ,  $\psi$ ,  $\omega$ ,  $\delta$ ,  $\epsilon$ ,  $\zeta$ ,  $\eta$ ,  $\theta$ ,  $\iota$ ,  $\kappa$ ,  $\lambda$ ,  $\mu$ ,  $\nu$ ,  $\xi$ ,  $\omicron$ ,  $\pi$ ,  $\rho$ ,  $\sigma$ ,  $\tau$ ,  $\upsilon$ ,  $\phi$ ,  $\chi$ ,  $\psi$ ,  $\omega$ ,  $\delta$ ,  $\epsilon$ ,  $\zeta$ ,  $\eta$ ,  $\theta$ ,  $\iota$ ,  $\kappa$ ,  $\lambda$ ,  $\mu$ ,  $\nu$ ,  $\xi$ ,  $\omicron$ ,  $\pi$ ,  $\rho$ ,  $\sigma$ ,  $\tau$ ,  $\upsilon$ ,  $\phi$ ,  $\chi$ ,  $\psi$ ,  $\omega$ ,  $\delta$ ,  $\epsilon$ ,  $\zeta$ ,  $\eta$ ,  $\theta$ ,  $\iota$ ,  $\kappa$ ,  $\lambda$ ,  $\mu$ ,  $\nu$ ,  $\xi$ ,  $\omicron$ ,  $\pi$ ,  $\rho$ ,  $\sigma$ ,  $\tau$ ,  $\upsilon$ ,  $\phi$ ,  $\chi$ ,  $\psi$ ,  $\omega$ ,  $\delta$ ,  $\epsilon$ ,  $\zeta$ ,  $\eta$ ,  $\theta$ ,  $\iota$ ,  $\kappa$ ,  $\lambda$ ,  $\mu$ ,  $\nu$ ,  $\xi$ ,  $\omicron$ ,  $\pi$ ,  $\rho$ ,  $\sigma$ ,  $\tau$ ,  $\upsilon$ ,  $\phi$ ,  $\chi$ ,  $\psi$ ,  $\omega$ ,  $\delta$ ,  $\epsilon$ ,  $\zeta$ ,  $\eta$ ,  $\theta$ ,  $\iota$ ,  $\kappa$ ,  $\lambda$ ,  $\mu$ ,  $\nu$ ,  $\xi$ ,  $\omicron$ ,  $\pi$ ,  $\rho$ ,  $\sigma$ ,  $\tau$ ,  $\upsilon$ ,  $\phi$ ,  $\chi$ ,  $\psi$ ,  $\omega$ ,  $\delta$ ,  $\epsilon$ ,  $\zeta$ ,  $\eta$ ,  $\theta$ ,  $\iota$ ,  $\kappa$ ,  $\lambda$ ,  $\mu$ ,  $\nu$ ,  $\xi$ ,  $\omicron$ ,  $\pi$ ,  $\rho$ ,  $\sigma$ ,  $\tau$ ,  $\upsilon$ ,  $\phi$ ,  $\chi$ ,  $\psi$ ,  $\omega$ ,  $\delta$ ,  $\epsilon$ ,  $\zeta$ ,  $\eta$ ,  $\theta$ ,  $\iota$ ,  $\kappa$ ,  $\lambda$ ,  $\mu$ ,  $\nu$ ,  $\xi$ ,  $\omicron$ ,  $\pi$ ,  $\rho$ ,  $\sigma$ ,  $\tau$ ,  $\upsilon$ ,  $\phi$ ,  $\chi$ ,  $\psi$ ,  $\omega$ ,  $\delta$ ,  $\epsilon$ ,  $\zeta$ ,  $\eta$ ,  $\theta$ ,  $\iota$ ,  $\kappa$ ,  $\lambda$ ,  $\mu$ ,  $\nu$ ,  $\xi$ ,  $\omicron$ ,  $\pi$ ,  $\rho$ ,  $\sigma$ ,  $\tau$ ,  $\upsilon$ ,  $\phi$ ,  $\chi$ ,  $\psi$ ,  $\omega$ ,  $\delta$ ,  $\epsilon$ ,  $\$

N a m e	data;0:1 <sup>00</sup> (L pc <sup>3</sup> )	data;10pc (L pc <sup>3</sup> )	m od;0:1 <sup>00</sup> (L pc <sup>3</sup> )	m od;10pc (L pc <sup>3</sup> )
E 240g12	27	59	5	8
E 317g20	172	211	1	1
E 482g17	40	52	3	4
E 498g5	134	813	37	93
E 499g37	63	43	10	7
E 508g34	0.7	1	0.4	0.4
E 548g10	198	198	14	14
E 548g29	42	64	4	5
E 549g18	62	91	7	9
E 572g22	40	74	0.7	0.8
N 1325	173	344	0.2	0.2
N 1345	41	80	44	66
N 1483	6	6	27	40
N 1640	1027	1431	8	9
N 2082	110	93	0.9	0.9
N 2196	498	900	995	1568
N 2344	1156	631	26	24
N 2460	981	1631	30	28
N 2758	79	193	491	1272
N 3045	31	87	1207	623
N 3054	318	423	1016	1689
N 3259	251	495	807	1305
N 3277	1559	1849	3	3
N 3455	267	221	6	6
N 3898	1311	1452	22	46
N 3900	1481	2531	317	713
N 3928	3900	2199	107	182
N 4030	861	861	131	232
N 406	3	4	1354	1620
N 4260	84	191	20	19
N 4384	6	—	18	17
N 4806	63	324	1578	1784
N 488	301	322	1629	3006
N 4980	1	2	1586	2883
N 5121	1704	2112	486	371
N 5985	129	485	151	151
N 6340	1425	1192	2	2
N 6384	224	350	176	272
N 7280	1829	2906	7	7
N 7421	513	859	1	1
N 7690	1184	1315	328	783
			2	2
			1647	2097
			2005	2575
			125	542
			1593	1335
			62	71
			1594	3041
			1800	3496
			218	346
			256	412
			1096	1205

Table 3: Stellar densities at 0:1<sup>00</sup> and 10 pc obtained from deprojecting the surface brightness profiles (subscript data) and the best fitting models of Table 2 (subscript mod). For the galaxies for which two best fits are available, the corresponding values for m od;0:1<sup>00</sup> and m od;10pc are reported following the same order as in Table 2.